

Interfacial “Single-Atom-in-Defects” Catalysts Accelerating Li⁺ Desolvation Kinetics for Long-Lifespan Lithium-Metal Batteries

Jian Wang,* Jing Zhang, Jian Wu, Min Huang, Lujie Jia, Linge Li, Yongzheng Zhang, Hongfei Hu, Fangqi Liu, Qinghua Guan, Meinan Liu, Henry Adenusi, Hongzhen Lin,* and Stefano Passerini*

The lithium-metal anode is a promising candidate for realizing high-energy-density batteries owing to its high capacity and low potential. However, several rate-limiting kinetic obstacles, such as the desolvation of Li⁺ solvation structure to liberate Li⁺, Li⁰ nucleation, and atom diffusion, cause heterogeneous spatial Li-ion distribution and fractal plating morphology with dendrite formation, leading to low Coulombic efficiency and depressive electrochemical stability. Herein, differing from pore sieving effect or electrolyte engineering, atomic iron anchors to cation vacancy-rich Co_{1-x}S embedded in 3D porous carbon (SAFe/CVRCS@3DPC) is proposed and demonstrated as catalytic kinetic promoters. Numerous free Li ions are electrocatalytically dissociated from the Li⁺ solvation complex structure for uniform lateral diffusion by reducing desolvation and diffusion barriers via SAFe/CVRCS@3DPC, realizing smooth dendrite-free Li morphologies, as comprehensively understood by combined in situ/ex situ characterizations. Encouraged by SAFe/CVRCS@3DPC catalytic promotor, the modified Li-metal anodes achieve smooth plating with a long lifespan (1600 h) and high Coulombic efficiency without any dendrite formation. Paired with the LiFePO₄ cathode, the full cell (10.7 mg cm⁻²) stabilizes a capacity retention of 90.3% after 300 cycles at 0.5 C, signifying the feasibility of using interfacial catalysts for modulating Li behaviors toward practical applications.

1. Introduction

The elevated demand for sustainable energy applications, such as electric vehicles, consumer electronics, and grid-energy storage systems, raises the necessity to develop superior high-energy-density lithium (Li) batteries.^[1] Compared to commercial graphite anode in Li-ion batteries, Li-metal anode displays unrivaled properties, specifically a high theoretical capacity (3860 mA h g⁻¹) and the most negative redox potential (−3.04 V vs standard hydrogen electrode).^[2] In spite of these features, the ultrahigh reactivity of Li-metal increases its propensity to react with solvent species or electrolyte salts in the solvation sheath, promoting unstable and loose solid electrolyte interphase (SEI) generation, severe Li-dendrite formation, and dead Li morphology, leading to low Coulombic efficiencies (CEs).^[2a,3] Meanwhile, the volumetric changes, breakage, and reformation of the unstable SEI consume the limited electrolyte, further shortening the cycle

J. Wang, S. Passerini
Helmholtz Institute Ulm (HIU)
D89081 Ulm, Germany
E-mail: jian.wang@kit.edu; stefano.passerini@kit.edu

J. Wang, M. Huang, L. Jia, L. Li, H. Hu, Q. Guan, M. Liu, H. Lin
i-Lab & CAS Key Laboratory of Nanophotonic Materials and Devices
Suzhou Institute of Nano-tech and Nano-bionics
Chinese Academy of Sciences
Suzhou 215123, P. R. China
E-mail: hzlin2010@sinano.ac.cn

J. Wang, S. Passerini
Karlsruhe Institute of Technology (KIT)
D-76021 Karlsruhe, Germany

J. Zhang
School of Materials Science and Engineering
Xi'an University of Technology
Xi'an 710048, P. R. China

J. Wu, F. Liu
College of Advanced Interdisciplinary Studies
National University of Defense Technology
Changsha 410073, P. R. China

Y. Zhang
State Key Laboratory of Chemical Engineering
East China University of Science and Technology
Shanghai 200237, P. R. China

 The ORCID identification number(s) for the author(s) of this article can be found under <https://doi.org/10.1002/adma.202302828>

© 2023 The Authors. Advanced Materials published by Wiley-VCH GmbH. This is an open access article under the terms of the Creative Commons Attribution License, which permits use, distribution and reproduction in any medium, provided the original work is properly cited.

DOI: 10.1002/adma.202302828

life.^[4] The uncontrollable dendrite growth during Li deposition would lead to internal short-circuit, overheating, or even fire.^[5]

To address these issues, current efforts are devoted to the protection of Li electrode surfaces by tuning SEI components and structures via electrolyte additives or artificial pre-treatments, or construction of 3D metal/carbon conductive skeletons to host Li.^[2b,3a,6] These strategies are aimed at either, changing the deposition morphology through the passivating interphase formation to separate Li from the electrolyte, or decreasing the current density of local deposition to eliminate large aggregation and dendrite generation.^[7] It is widely accepted that the Li plating processes involve a series of interfacial Li transport steps such as Li⁺ transfer across the SEI, diffusion/migration of Li⁺ or Li⁰ along the electrode surface or inside the hosts, and nucleation and growth of Li⁰ deposits.^[1a,8] However, the dissociation of the Li⁺ solvation structure for releasing free Li⁺ at the interface plays a decisive role in the subsequent solid-state diffusion and redistribution of Li⁺ and Li⁰. Previous studies have demonstrated that dissociating Li⁺ by removing the bound solvents from the primary solvation sheath was beneficial for the formation of free Li⁺.^[6k,9] Common strategies to regulate the Li⁺ solvation environment mainly focus on electrolyte tuning, that is, adopting high-concentration electrolytes (HCEs) to modulate the solvation structure, or sieving appropriate solvated Li ions through the pores of metal–organic frameworks (MOFs).^[10] However, the high cost and electrochemical stability of HCEs and MOFs in the organic electrolyte prevent wide application. Furthermore, the optimizations of the Li⁺ solvation structure by tuning the electrolyte concentration or components do not guarantee the rapid dissociation of the complex to release free Li⁺ at the electrode/electrolyte interface, since the complex is generally formed by replacing a part of the coordinated solvent molecules with anions or other more strongly bound species.^[5b,10f] Actually, the desolvation of the Li⁺ solvation structure can be regarded as a decomposition reaction with a specific energy barrier, which is often so large that the interfacial desolvation becomes the rate-limiting step during the interfacial Li⁺ transfer and diffusion.^[11] Therefore, the Li⁺ solvation behavior might be modulated by introducing active catalysts into the systems.

Single-atom catalysts (SACs) uniformly dispersed in a nanostructured matrix, exhibiting ideal atom exposure of 100%, are capable of serving as kinetic promoters to impel conversion reactions with high utilization efficiency and activity.^[12] Compared with the widely-adopted nitrogen-doped nanocarbon as an SAC supporter via metal-N_x bonding, defect-rich metal compounds

(DMC) with tunable electronic state structures can also serve as supporters by mounting single atoms of the desired metal onto the defect sites (SAC-in-Defects).^[13] In our previous works, we successfully demonstrated the application of nanocarbon- or DMC-supported SACs in improving the Li exchanging and diffusion kinetics to achieve high-performance sulfur cathodes and dendrite-free Li-metal anodes.^[8b,c,12a,14] The local defect sites could regulate the intrinsic electronic density distribution and liberate strong atomic metal-defect interactions, which is beneficial not only for stabilizing the SACs and improving their distribution homogeneity but also for improving the activity of each SAC site.

Herein, differing from the widely adopted solvation sheath tuning strategy, Li⁺ desolvation and Li⁰ atom diffusion kinetics against dendrite growth are boosted catalytically by employing an interfacial catalyst layer composed of SAC-in-Defects on metallic Li. As a prototype of the SAC-in-Defects material, single iron atoms are anchored onto cation vacancy-rich cobalt sulfide (Co_{1-x}S) nanoparticles distributed within the 3D architecture of porous carbon (SAFe/CVRCS@3DPC), acting as kinetic promoters. The impacts of rapid desolvation on interfacial Li⁺ and Li⁰ transport kinetics for achieving dendrite-free and high-performance Li-metal anodes are characterized through comprehensive electrochemical analysis, in situ sum frequency generation (SFG) and Raman spectroscopies, together with theoretical calculations. Consequently, the modified Li-metal electrode (SAFe/CVRCS@3DPC-Li) displays the rapid ability to generate free Li⁺ from complex desolvation and atom diffusion, achieving smooth, dendrite-free, and long-term Li plating with a cycle life of 1600 h. Paired with the high-loading LiFePO₄ cathode (10.67 mg cm⁻²), the fabricated full cell delivers an ultrahigh capacity of 131 mA h g⁻¹ after 300 cycles at 0.5 C, demonstrating the viability of SAFe/CVRCS@3DPC for practical application.

2. Results and Discussion

2.1. DFT Calculations of Li⁺ Desolvation Behavior Catalyzed by SAC

First, the stability of atomic iron in the defect sites of CVRCS was identified by density functional theory (DFT) calculations (Figure 1A,B).^[13a,b] The Fe single atoms located at Co atom vacancies possess much lower free energy than those anchored to other sites in the CoS crystal lattice (Figure 1B), strongly suggesting the feasibility of constructing the “SAC-in-Defects” structure. In the practical systems, both Li(1,3-dioxolane)_n⁺ (Li(DOL)_n⁺) and Li(1,2-dimethoxyethane)_n⁺ (Li(DME)_n⁺) may exist in the bulk or electrolyte interface. To reveal how the SAFe/CVRCS propels dissociation of Li⁺ from its solvation structure and Li⁰ diffusion on the surface, the reduction potentials of differing solvated Li ions in the formation of Li(DME)_n⁺ and Li(DOL)_n⁺ (*n* = 1, 2, 3, and 4) were calculated (Figure 1C–K; Figures S1–S7, Supporting Information).^[10f] The greater the coordination number of Li⁺, the higher the desolvation barrier that must be overcome (Figure 1D; Figure S2, Supporting Information), ranging from 0.65 to 3.33 eV for *n* in Li(DME)_n⁺ complex from 1 to 4 (Figure 1D). Li(DME)₄⁺, a primary symmetric species at the electrode/electrolyte interface, was found to

H. Adenusi
The University of Hong Kong
Department of Chemistry
Hong Kong P. R. China
H. Adenusi
Hong Kong Quantum AI Lab
17 Science Park West Avenue, Hong Kong P. R. China
S. Passerini
Sapienza University of Rome
Chemistry Department
P. A. Moro 5, Rome 00185, Italy

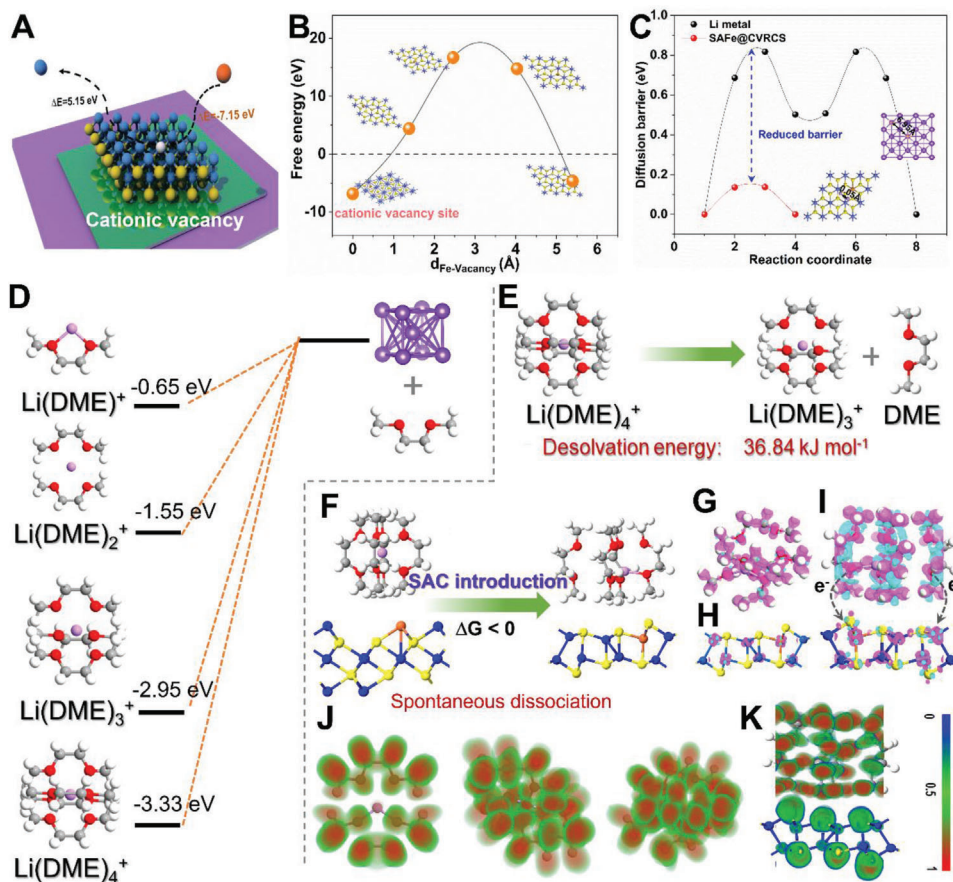


Figure 1. Stability of SAC-in-Defects and its propensity to rapidly propel Li^+ desolvation and atom diffusion using theoretical calculations. A) Schematic illustration of replacing Co atom by Fe atom in the vacancy site and B) the corresponding free energy of Fe atom in different sites. C) Comparison of lithium atom diffusion barrier on the surface of metallic Li or SAFe/CVRCS, respectively. D) Reduction energy of Li solvation complex, that is, $\text{Li}(\text{DME})_n^+$ calculated by DFT. E,F) Desolvation barrier of $\text{Li}(\text{DME})_4^+$ into $\text{Li}(\text{DME})_3^+$ and DME in liquid electrolyte (E) or on SAFe/CVRCS (F), respectively. G–I) The corresponding differential electron density transfer of $\text{Li}(\text{DME})_4^+$ (G), SAFe/CVRCS substrate (H), and $\text{Li}(\text{DME})_4^+$ on SAFe/CVRCS, respectively. J,K) Electron localization function states of solvated $\text{Li}(\text{DME})_n^+$ species in the electrolyte (J) or SAFe/CVRCS (K), respectively.

require a higher reduction potential to drive its decomposition into $\text{Li}(\text{DME})_3^+$ and free DME molecule (Figure 1E), corresponding to a dissociation energy barrier of $\approx 36.84 \text{ kJ mol}^{-1}$. In the presence of SAFe/CVRCS, both the DME molecule and DOL molecule coordinated to the central Li^+ in the $\text{Li}(\text{DME})_4^+$ or $\text{Li}(\text{DOL})_4^+$ complex tend to move to the SAFe/CVRCS surface and suggest these desolvations proceed spontaneously ($\Delta G < 0$) to release Li ions without costing additional energy (Figure 1F; Figure S3, Supporting Information). To further understand SAFe/CVRCS behavior during the desolvation process, the differential electron density and the electron localization function of the two systems with/without SAFe/CVRCS substrate were investigated (Figure 1G–K; Figures S4 and S5, Supporting Information).^[15] In the pristine $\text{Li}(\text{DME})_n^+$ or $\text{Li}(\text{DOL})_n^+$ molecular system, the electronic states are mainly concentrated around the Li^+ center (Figure 1G), while the electrons are transferred to the catalyst surface after introducing SAFe/CVRCS into the system in comparison with the SAFe/CVRCS substrate (Figure 1H,I; Figures S4 and S5, Supporting Information), leading to the solvents dissociation from the Li^+ solvation sheath.

On the other hand, as shown in the electron localization function of Figure 1J,K, the binding environment of $\text{Li}(\text{DME})_n^+$ has changed from strongly to weakly coordinating upon the introduction of SAFe/CVRCS, implying the decreased desolvation barriers of bonded $\text{Li}(\text{solvents})^+$. A similar phenomenon is also found in the $\text{Li}(\text{DOL})_n^+$ system. Once coupled with electrons at the electrode surface, the free Li ion converts into atomic Li, that is, the Li^0 atom. To understand how the Li^0 atom diffuses, the atom diffusion capability on the pristine metallic Li surface and on the SAFe/CVRCS surface were also compared (Figure 1C).^[8a,16] According to a similar approach described in our previous study, the dimer model was used and the adsorbed structures were optimized (Figure S7, Supporting Information).^[8a] The Li^0 atom on the pristine Li surface is hard to diffuse because of the high barrier of 0.82 eV. In contrast, the Li atom is easy to diffuse around the SAFe localized site with barriers of 0.14 eV, ≈ 6 times lower than that on metallic Li surface, confirming the significant contributions of the SAFe/CVRCS@3DPC in promoting Li^0 atom diffusion for further lateral electroplating without any vertical dendrite growth.

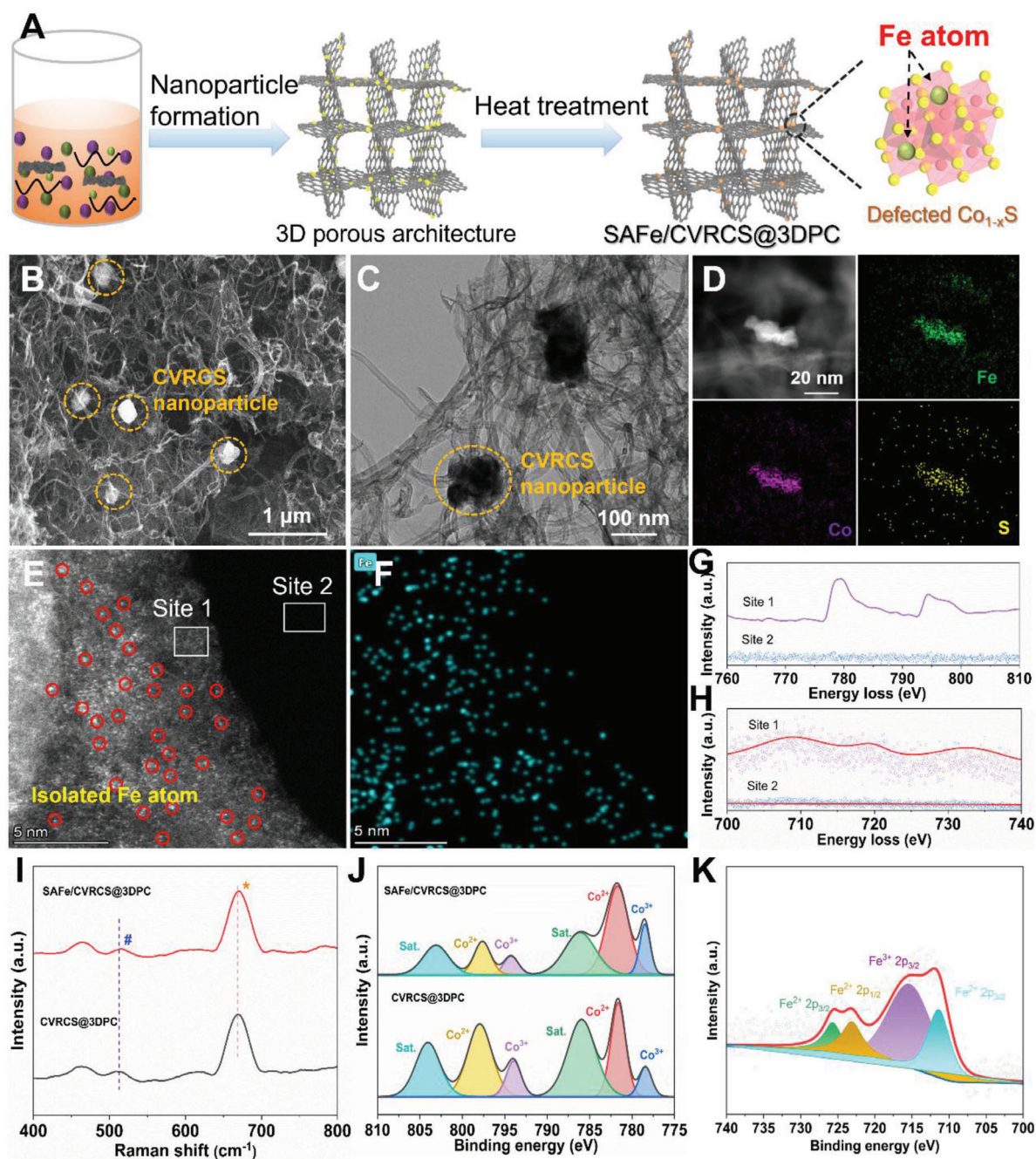


Figure 2. Morphology and characterizations of SAFe/CVRCS@3DPC catalyst. A) Schematic synthesis of the SAFe/CVRCS@3DPC. B) SEM image, C) TEM images, and D) EDX elemental mappings of the SAFe/CVRCS@3DPC; E) HAADF-STEM image of SAFe/CVRCS@3DPC and F) the corresponding Fe atom mapping (the bright dots in 2E represent the Fe atom). G, H) Electronic energy loss spectroscopy comparison of Co (G) and Fe (H) in the selected areas in 2E. I) Comparisons of Raman spectra of SAFe/CVRCS@3DPC and CVRCS@3DPC nanocomposites, respectively. J) XPS spectra of Co 2p in the composite with/without SAFe. K) High-resolution Fe 2p in the SAFe/CVRCS@3DPC nanocomposite.

2.2. Morphology/Structural Characterizations of “SAC-in-Defects” Catalyst

Figure 2A depicts the schematic synthesis illustration of SAFe/CVRCS@3DPC via hydrothermal and heating reactions. Then, the presence and states of atomic iron in defected Co_{1-x}S are further comprehensively verified by experimental charac-

terization techniques including elemental mapping, atomic resolution high-angle annular dark-field spherical-aberration-corrected transmission electron microscopy (HAADF-STEM) and electronic energy loss spectroscopy (EELS). The scanning electron microscopy (SEM) image of SAFe/CVRCS@3DPC in Figure 2B displays that the synthesized nanoparticles are placed on the cross-linked porous network. As revealed by transmission

electron microscopy (TEM), the SAFe/CVRCS@3DPC nanocomposite presents the aggregated Co_{1-x}S nanoparticles with a size of ≈ 100 nm (Figure 2C).^[8b] The energy-dispersive X-ray (EDX) spectrum and mappings of SAFe/CVRCS@3DPC in Figure 2D and Figure S8 (Supporting Information) confirm that the distribution of Fe element coincides with that of the Co and S elements. Further, atomic resolution HAADF-STEM was performed to visualize the atom presence of elemental Fe in the SAFe/CVRCS@3DPC (Figure 2E,F).^[2c,17] Consistent with the atom mapping in Figure 2F, isolated bright spots highlighted with red circles are observed in the HAADF-STEM image (Figure 2E), suggesting uniform atom dispersion without any aggregation. As expected, the characteristic signals of Co and Fe corresponding to the selected area in Figure 2E are well recorded in Figure 2G,H by EELS. In comparison to Site 2, the signals of Fe and corresponding Co elements in Site 1 indicate that the single iron atoms are mainly anchored separately in the CVRCS rather than in the carbon matrix. These results of HAADF-STEM, atomic mapping, and EELS depict the successful fabrication of the “SAC-in-Defects” structure.

Apart from the diffraction peaks of the Co_{1-x}S (JCPDS card No.42-0826), no Fe–Fe cluster or iron–cobalt binary compounds were detected in the SAFe/CVRCS@3DPC (Figure S9, Supporting Information), consistent with the HAADF-STEM and EELS results. The three Raman peaks centered ≈ 463 , 512, and 668 cm^{-1} in the two samples match with the stretching modes of Co_{1-x}S (Figure 2I).^[18] With the loading of SAFe, the peaks attributed to the asymmetric vibration of CVRCS shift to a higher wavenumber. Also, a slight increase of the I_D/I_G ratio from 0.93 to 0.99 is revealed, indicating more defects in nanocarbon induced by the redistribution of localized electronic distribution of carbon atom in the surrounding delocalized electronic density in SAFe/CVRCS@3DPC (Figure S10, Supporting Information).^[19] In the high-resolution X-ray photoelectron spectroscopy (XPS) of Co 2p spectra in the SAFe/CVRCS@3DPC (Figure 2J), the first pair of peaks located at 778.68 and 781.88 eV are related to $\text{Co}^{3+} 2p_{3/2}$ and $\text{Co}^{2+} 2p_{3/2}$ while the other pair of peaks at 793.98 and 797.98 eV are assigned to $\text{Co}^{3+} 2p_{1/2}$ and $\text{Co}^{2+} 2p_{1/2}$, respectively.^[12a,17b] The dominant intensity of Co^{2+} implies the significant variation of bonding coordination of Co centers with the implantation of SAFe. Meanwhile, another two peaks positioned at 161.2 and 163.8 eV are assigned to metal–sulfur bonds (Figure S11, Supporting Information).^[20] The anchored SAFe is also inspected by XPS with the typical $\text{Fe}^{2+} 2p_{3/2}$ and $\text{Fe}^{2+} 2p_{1/2}$ species at 711.5 and 723.18 eV (Figure 2K).^[21] evidently showcasing the presence of SAFe in the CVRCS.

2.3. Li^+ Desolvation Behaviors Probed by in situ SFG and Raman Spectroscopies

The net desolvation process takes place at the electrode/electrolyte interface instead of the bulk electrolyte interior.^[1a] Thanks to the interface-sensitive SFG spectroscopy, the desolvation behaviors of the solvated Li^+ were dynamically observed with/without plating bias voltage (Figure 3).^[22] As illustrated in Figure 3A, the in situ SFG spectroelectrochem-

ical cell was configured so that the pulse lights can reach the electrode/electrolyte interface accurately.^[23] Figure 3B,C schematically depict the status of the Li^+ solvation structure at the electrode/electrolyte interface under the conditions of open-circuit voltage state or bias voltage. Generally, the interfacial solvent behavior in the solvation shell has a close relationship with the electrode surface state at the interface. Apparent solvent peaks of C=O bond assigned to solvents are observed at ≈ 1592 , 1720, and 1790 cm^{-1} either in/out of the SAC modulation layer (Figure 3D).^[6f,23,24] Meanwhile, the typical C–H bond vibrations in the region between 2750 and 3050 cm^{-1} were also detected in the systems with/without SAC (Figure 3E), indicating the presence of solvents at the electrode/electrolyte interface.^[25] Upon applying a bias voltage of 20 mV onto the systems (Figure 3C), the dynamic process of dissociating the Li^+ -solvents is initially proceeding at the interface with different reaction kinetics. Compared with the initial states on 3DPC or SAFe/CVRCS@3DPC, the solvent peak position in the SFG spectroscopy remains similar, (unchanged before and after applying bias voltage), thus the behaviors of Li^+ -solvent complex are not altered (Figure 3F,G). In sharp contrast, both the SFG intensities of the C=O and C–H vibrations were substantially reduced at the SAFe/CVRCS@3DPC//electrolyte interface (Figure 3F,G). In the case of SAFe/CVRCS@3DPC, the intensity decrease of the peaks driven by the bias voltage is undoubtedly attributed to the dissociation of the Li^+ solvation complex catalyzed by SAFe/CVRCS@3DPC, since the controlled 3DPC sample with similar surface morphology did not show obvious intensity decrease under the same condition. Owing to the same signal contributions of free solvents in the systems before and after applying voltage bias, the reduction of SFG intensity is assigned to the catalytic functions of SAFe/CVRCS@3DPC in dissociating Li^+ -solvents. In the ex situ Raman spectra, the higher intensity ratio of contact ion pairs (CIP) and aggregates (AGG) in the electrolyte interior indicates the depth of desolvation for a high concentration of free Li^+ anions (Figure 3H).^[9] The sum intensities of AGG and CIP exhibit higher than pristine electrolyte upon contacting with the SAFe/CVRCS@3DPC catalytic layer (Figure 3I), similar to the desolvation behaviors in the HCE, forming many free Li^+ ions after fast desolvation catalyzed by SAFe/CVRCS@3DPC (Figure 3J). Above all, the SFG and Raman spectroscopy results have demonstrated the SAFe/CVRCS@3DPC to be beneficial for propelling desolvation kinetics at the electrode/electrolyte interface by lowering desolvation barriers to free a greater proportion of Li^+ ions.

2.4. Dendrite-Free Li Electroplating Performance on SAFe/CVRCS@3DPC-Li Anodes

A thin SAFe/CVRCS@3DPC catalytic layer was filtered on commercial separators with a thickness of $\approx 5\text{ }\mu\text{m}$ for stimulating Li plating kinetics (Figure S12, Supporting Information). Figure 4A displays that the symmetric cell with SAFe/CVRCS@3DPC catalytic layer shows reduced charge transfer resistance and enhanced mass transfer kinetics.^[26] Meanwhile, according to the reported formula, the SAFe/CVRCS@3DPC modified Li (SAFe/CVRCS@3DPC-Li) displays a dramatically lower diffusion resistance with a

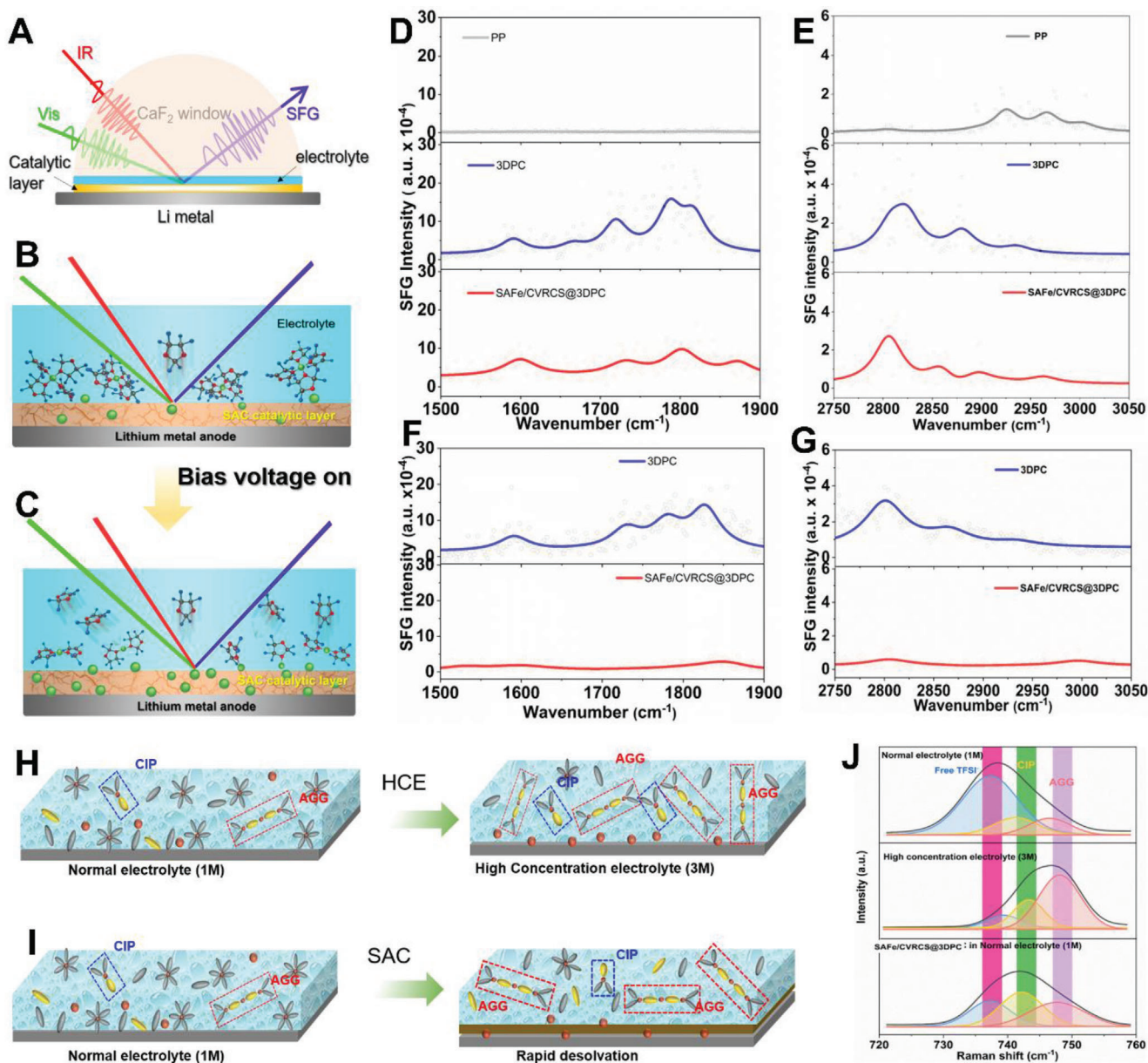


Figure 3. In situ and ex situ spectroelectrochemical characterizations showcasing accelerated interfacial Li^+ dissociation catalyzed by SAFe. A) Schematic illustration of the in situ SFG probing the electrolyte/catalyst interface. B,C) The molecular states of the Li^+ solvation structure in the electrode/electrolyte interface before (B) and after (C) turning the bias voltage on. D,E) The SFG spectra of different adsorption states of Li^+ solvation structure under the C–O region (D) and C–H region (E), respectively. The decreased SFG intensities in F) the C–O region and G) C–H region with/without introducing SAFe under the bias of 20 mV, respectively. H,I) Schematic illustration of further depleting solvent molecules in the HCE (H) and on the catalytic surface (I). J) Comparison of the corresponding Raman spectra of the interface and electrolyte.

smaller fitting slope than pristine Li (0.72 vs 5.48) (Figure 4B), indicating the fast transportation of the generated free Li^+ .^[6d,f] The nucleation barrier was then evaluated on asymmetric Li–Cu cells, and the SAFe/CVRCS@3DPC–Cu electrode significantly decreases the nucleation barrier to as low as 29 mV in contrast to that of the pristine Cu electrode (102 mV) at 0.5 mA cm^{-2} (Figure 4C), which also coincides with the expectation of fast dissociation of the Li^+ solvation structure under the catalysis of SAFe/CVRCS@3DPC. The nucleation rate is roughly estimated to be increased by ≈ 34 times, implying the boosted catalytic

capability of the SAC-in-Defects structure. In the successive plating/stripping, the SAFe/CVRCS@3DPC–Cu electrode displays remarkably more stable CEs for 120 cycles (Figure 4D), whereas the pristine Cu undergoes an up-and-down tendency after 60 cycles and then decays to a failure state in the later cycles. Enlarging the current density to 1.0 mA cm^{-2} , a reduced barrier and enhanced CEs recur under the SAFe/CVRCS@3DPC modulation (Figure S13, Supporting Information). The rapid desolvation of Li^+ and fast Li^0 atom diffusion are also reflected in the Li–Li symmetric cells. Figure 4E depicts the voltage curves of

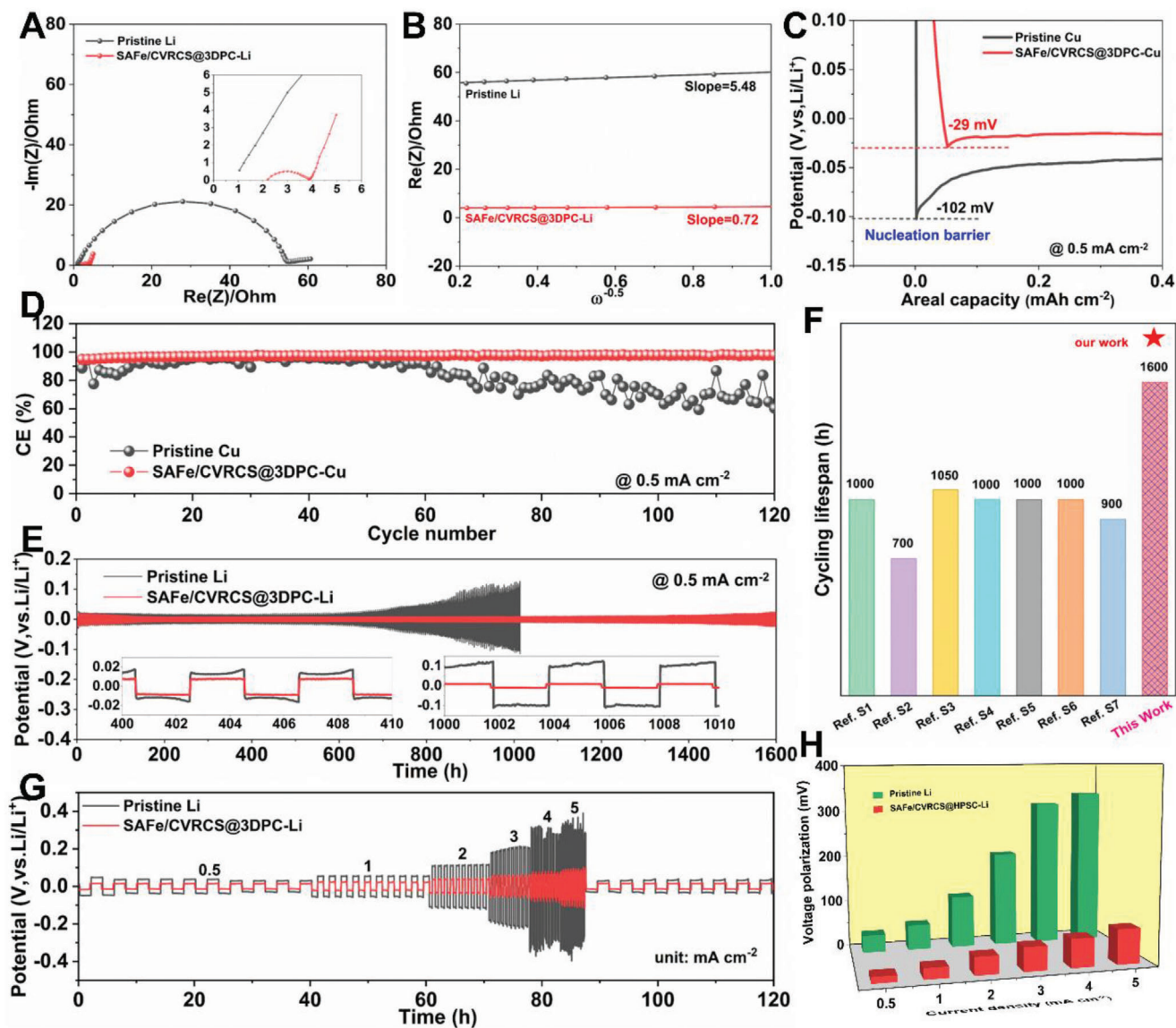


Figure 4. Dendrite-free Li plating performance with SAFE/CVRCS@3DPC. A,B) Comparisons of EIS (A) and Li-ion transport (B) with/without SAFE. C) Comparison of Li nucleation on the pristine Cu or SAFE/CVRCS@3DPC-modified Cu at 0.5 mA cm^{-2} . D) Comparison of successive CE for the two asymmetric cells at 0.5 mA cm^{-2} . E) Galvanostatic plating/stripping stability of the SAFE/CVRCS@3DPC-Li and pristine Li electrodes at 0.5 mA cm^{-2} (inset: the enlarged specific voltage from 400 to 410 and 1000 to 1010 h, respectively). F) Lifespan comparison between our study and the recently reported literature. G) Comparisons of rate performance and H) corresponding voltage gaps of the two electrodes at specific current densities.

the SAFE/CVRCS@3DPC-Li cell, and it is capable of enduring cyclic stability over 1600 h without any short-circuiting. In sharp contrast, the pristine Li only survives for ≈ 700 h before forming “dead Li” and/or growing Li dendrites. As highlighted in the inset, the overpotentials of SAFE/CVRCS@3DPC-Li electrode maintain as low as 18 mV constantly, while the overpotentials of the pristine Li electrode reach two times higher at 400 h and rapidly increase more than 220 mV after 1000 h (Figure 4E). During the stripping/plating process, the Co_{1-x}S matrix may react with Li to generate a partially lithiated state with the formula of $\text{Li}_z\text{Co}_{1-x}\text{S}_y$. Such a partially lithiated state is expected to be beneficial for Li^+ transport due to the increased number of Li-ion transport pathways. As the defect sites

in partially lithiated $\text{Li}_z\text{Co}_{1-x}\text{S}_y$ are similar to that in Co_{1-x}S , the atomic state of the SAFE and its catalytic activity are expected to be maintained after the partial lithiation. Cycled at 2 mA cm^{-2} , the SAFE/CVRCS@3DPC-Li electrode also manifests stable overpotentials and long lifespans for 450 h (Figure S14, Supporting Information), respectively, implying that the SAFE/CVRCS@3DPC catalytic layer makes significant catalytic contributions in improving the Li-metal anode performances. In comparison to the state-of-the-art electrode reports (Table S1, Supporting Information), the SAFE/CVRCS@3DPC-Li electrode presents a competitively longer lifespan (Figure 4F). It is worth noting that the SAFE/CVRCS@3DPC-Li can still maintain a relatively small overpotential ≈ 73 mV, even when

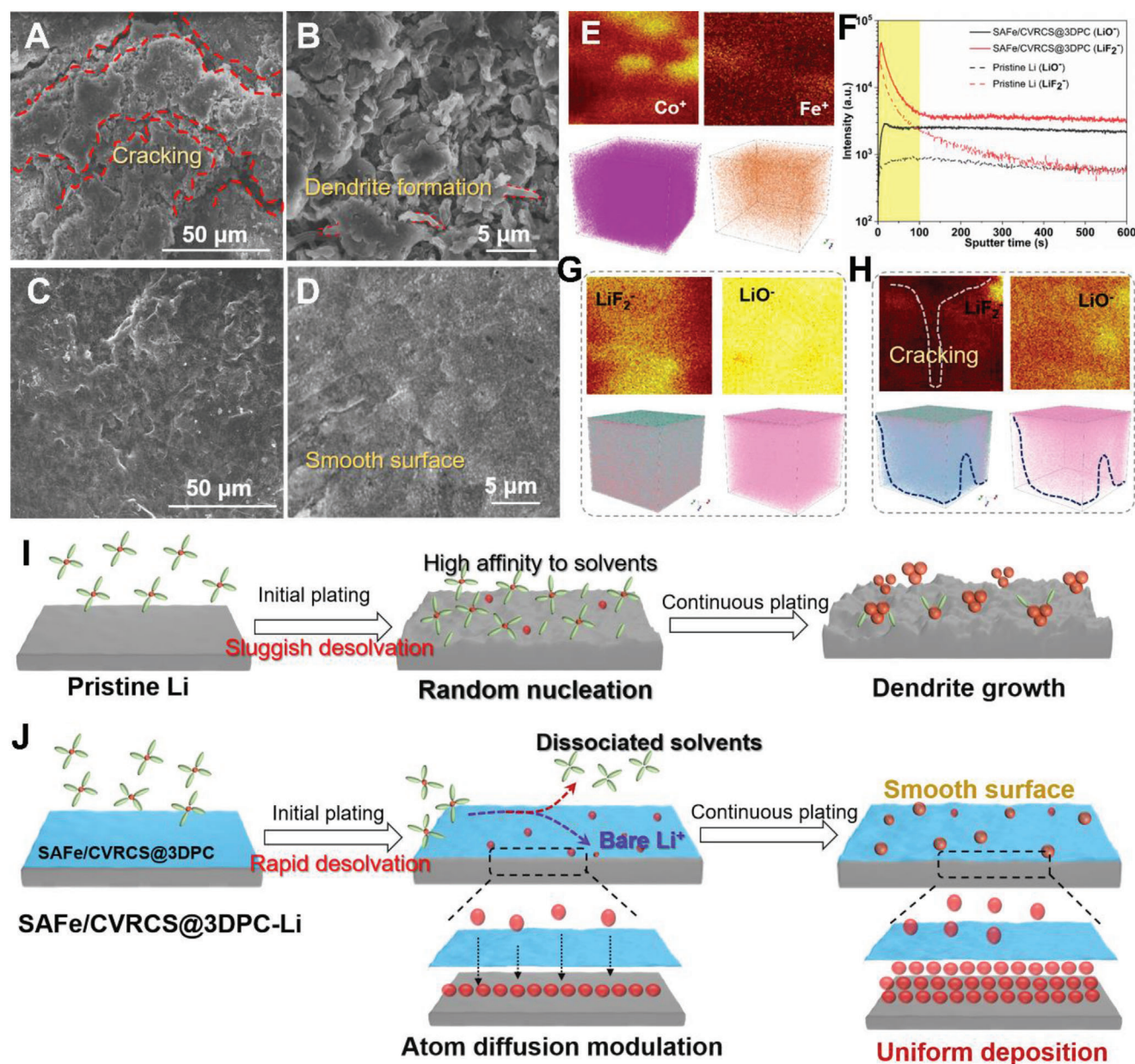


Figure 5. Mechanism of SAFe/CVRCS@3DPC in manipulating lateral lithium electroplating behaviors. A) Low-resolution and B) high-resolution SEM images of cycled pristine Li electrode. C) Low-resolution and D) high-resolution SEM images of cycled SAFe/CVRCS@3DPC-Li electrode. E) Surface and 3D reconstruction of Co^+ and Fe^+ in the catalytic layer after cycling. F) Intensity comparison of Li^+ species in pristine Li or cycled modified Li. G, H) Surface and 3D reconstruction of Li^+ species in modified Li (G) and pristine Li with cracking (H). I, J) Schematic illustration of lithium plating behaviors on pristine Li (I) and catalytic SAFe/CVRCS@3DPC layer (J) in propelling desolvation and atom diffusion for lateral deposition.

the current density reaches as high as 5 mA cm^{-2} , much lower than that of the pristine Li (334 mV) under the same condition (Figure 4G,H). Decreasing the current density back to 0.5 mA cm^{-2} , the plating/stripping potential returns to only $\approx 20 \text{ mV}$ (Figure 4G). Such excellent reversibility and robustness should be attributed to the functions of single iron atoms in accelerating the desolvation of Li^+ and promoting Li^0 atom horizontal diffusion toward smooth plating instead of vertical Li-dendrite growth.

2.5. Mechanisms of SAFe/CVRCS@3DPC in Modulating Li-Ion/Atom Diffusion

To directly observe the enhanced Li^0 atom diffusion morphology by the SAFe/CVRCS@3DPC promoter, ex situ SEM images were recorded (Figure 5A–D; Figure S15, Supporting Information). Mossy lithium growth and characteristic cracking are evident in Figure 5A and the formation of sharp Li dendrites is observed as circled in the high-resolution SEM image (Figure 5B).^[3d] On

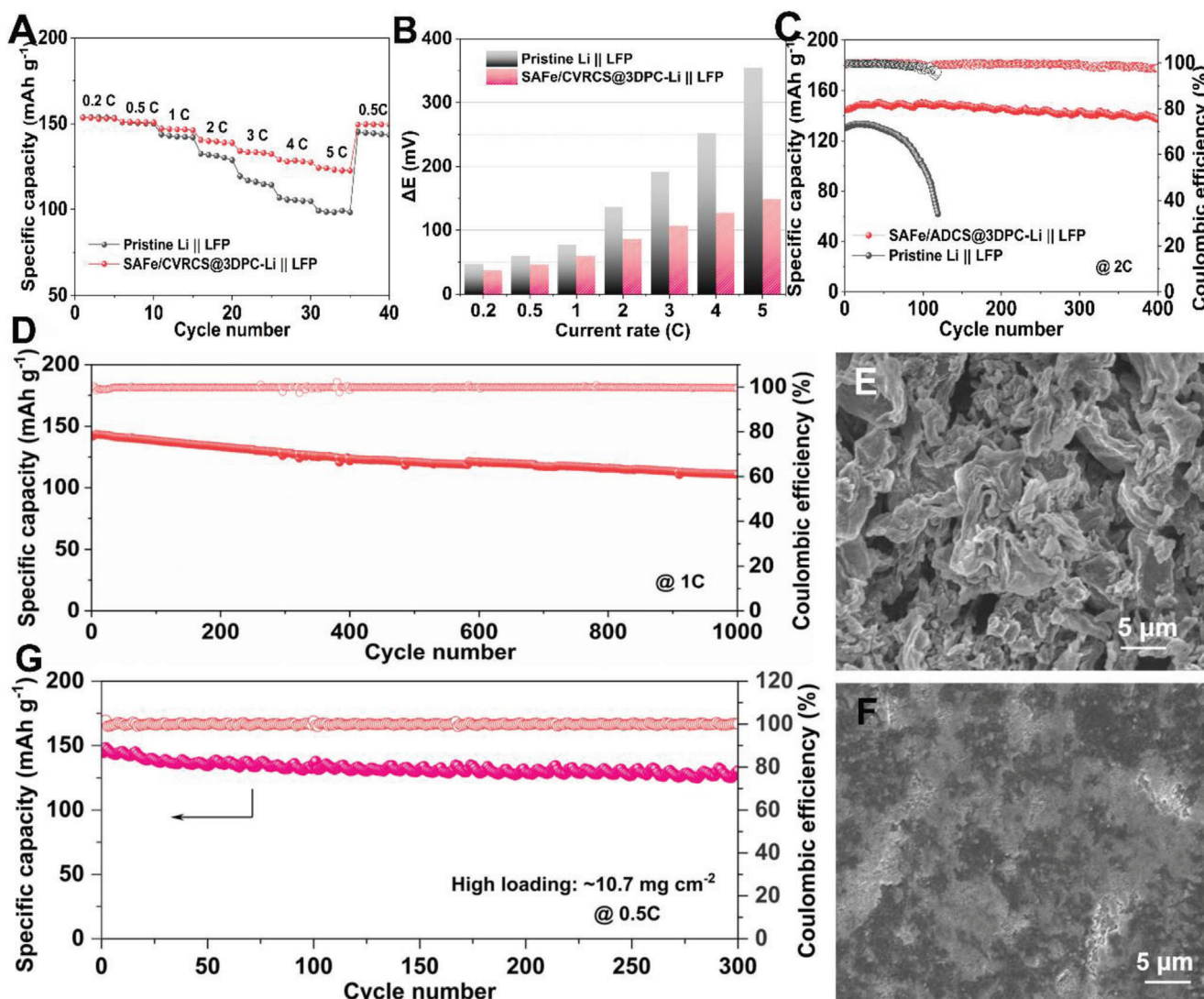


Figure 6. Electrochemical performance of full batteries based on the SAFe/CVRCS@3DPC-Li promoter. A–C) Comparisons of rate performance (A), corresponding potential gaps (B), and cycling stability at 2 C (C) of the two full cells with/without SAFe/CVRCS@3DPC promoters. D) Cycling performance of SAFe/CVRCS@3DPC-Li || LFP cell at 1 C for 1000 cycles. E,F) High-resolution SEM images of pristine Li (E) and modified Li (F) in the cycled full battery. G) The stability investigation of the high-loading full cell up to 10.7 mg cm^{-2} with the modulation of SAFe/CVRCS@3DPC promoter in the Li anode.

the contrary, the SAFe/CVRCS@3DPC modulated Li electrode presents a relatively smooth plating surface without any dendrite in the low or high-resolution SEM image (Figure 5C,D). Compared with the pristine catalytic layer, the thickness increases very little and remains $\approx 7 \mu\text{m}$, this is also indicative that the Li atom is hard to plate within the SAFe/CVRCS@3DPC modulation layer (Figure S15, Supporting Information). Further, the 3D morphology and species distributions are examined by time-of-flight secondary-ion mass spectrometry (TOF-SIMS).^[6f,8a] The Co^+ species ascribed to CVRCS is well-distributed without large aggregation in the bulk of the SAFe/CVRCS@3DPC (Figure 5E). Meanwhile, the Fe^+ species are correspondingly located on the CVRCS, strongly demonstrating the defect-site anchored atomic structure of Fe after plating/stripping. Much higher intensities of the Li-related species are achieved on the surface along with

the increase of sputter time (Figure 5F,G), representing more Li-related resources on the modulated Li surface. In contrast to the obvious crack and dendrite in the pristine Li, smooth and uniform Li surface, and a bulk layer of well-distributed plated Li are observed for the SAFe/CVRCS@3DPC modulated Li electrode, as displayed in Figure 5H.

In the pristine Li, the solvents in partially desolvated Li^+ tend to deposit and form random nucleation owing to the high affinity. In the continuous plating, the loose turbulent sites give rise to the formation of Li dendrites, inducing dead Li formation and causing limited electrolytes (Figure 5I). Upon reaching the catalytic modulation layer, the Li^+ solvation shell is immediately dissociated to generate free Li^+ and free solvent species, as revealed by in situ/ex situ spectroscopical measurements and DFT calculations (Figure 5J). Afterward, the free Li ion flux diffusion is

further regulated by the SAFe/CVRCS and preferentially diffuses horizontally along the SAFe/CVRCS@3DPC modulation layer after coupling with electrons. Therefore, the Li ions/atoms are uniformly plated on the surface instead of growing vertically to form a rugged surface or even dendrites analogous to the pristine Li surface, leading to a superior lifespan and high utilization.

2.6. Electrochemical Performance of Full Batteries Based on SAFe/CVRCS@3DPC-Li

The functions of the SAFe/CVRCS@3DPC are further evaluated in Li-LiFePO₄ full cells. The fresh full cell based on SAFe/CVRCS@3DPC-Li possesses the lower charge-transfer resistance (6.5 vs 47.5 Ω) and higher lithium ions diffusion kinetics (Figure S16, Supporting Information).^[27] The modified full cell delivers reversible rate capacities of 140 and 123 mA h g⁻¹ at 2 C and 5 C, respectively (Figure 6A). Meanwhile, much lower overpotentials are realized in the SAFe/CVRCS@3DPC-modified full cells, especially under high current density (Figure 6B; Figure S17, Supporting Information). Additionally, the modified cell retains the capacity of 137 mA h g⁻¹ after 400 cycles at 2 C (Figure 6C). In the long-term cycling, the SAFe/CVRCS@3DPC-modulated full cell maintains for 1000 cycles with a fading rate of 0.030% per cycle at 1 C (Figure 6D). After cycling, in comparison to the dendrite analogs and ruptured dead lithium on the pristine Li surface (Figure 6E; Figure S18A, Supporting Information), a smooth and dense Li-metal surface highlights the effectiveness of the SAFe/CVRCS@3DPC in promoting desolvation and atom diffusion (Figure 6F; Figure S18B, Supporting Information). In the high-mass-loading LiFePO₄ cathode up to ≈10.7 mg cm⁻², the modified cell stabilizes the capacity of 131 mA h g⁻¹, corresponding to a capacity retention of 90.3% after 300 cycles (Figure 6G), which is superior to most reports (Table S2, Supporting Information). Meanwhile, the high-loading full cell also exhibits stable voltage potential gaps during the entire discharging/charging process (Figure S19, Supporting Information). For potential commercialization, the high-capacity full cell with a thin Li foil electrode was also investigated. Even decreasing the Li foil thickness down to 50 μm, the high-loading cell still stabilizes the capacity of 139 mA h g⁻¹ after 100 cycles (Figure S20, Supporting Information), highlighting the advantages of SAC in dissociating Li⁺-solvents and lateral atom diffusion for smooth plating.

3. Conclusion

To promote the dissociation of the Li⁺ solvation structure to release free Li ions and the diffusion of the Li⁰ atom, a catalytic strategy of “SAC-in-Defects” is implemented to reduce the desolvation and diffusion barriers. This facilitates homogeneous Li seeding and successive uniform Li plating, as comprehensively elucidated by in situ/operando characterizations and theoretical calculations. Consequently, the prototype SAFe/CVRCS@3DPC catalytic layer significantly increases the nucleation rate up to ≈34 times higher, contributing to dendrite-free lithium deposition with a lifespan of up to 1600 h and high CE without any short-circuit. The paired high-loading cell (≈10.7 mg cm⁻²) maintains

a capacity retention of 90.5% after 300 cycles. This work provides new insights into adopting active catalysts to accelerate desolvation, nucleation, and atom diffusion for practical lithium-metal batteries.

Supporting Information

Supporting Information is available from the Wiley Online Library or from the author.

Acknowledgements

J.W., J.Z., J.W., and M.H. contributed equally to this work. The authors acknowledge the National Key R&D Program of China (2021YFA1201503), the Natural Science Foundation of Jiangsu Province (BK 20210130), the National Natural Science Foundation of China (No. 21972164; 22279161; 22075313), Innovative and Entrepreneurial Doctor in Jiangsu Province (JSSCBS20211428), and Shaanxi Natural Science Basic Research Plan (No. 2022JQ-137). J.W. and S.P. acknowledge the financial support from the Alexander von Humboldt Foundation and the basic funding of the Helmholtz Association. H.A. acknowledges the University of Hong Kong and the Hong Kong Quantum AI Lab Limited for supporting his fellowship and honorary positions. The authors also thank the scientific-technical support from Nano-X in Suzhou Institute of Nano-tech and Nano-bionics, Chinese Academy of Sciences.

Open access funding enabled and organized by Projekt DEAL.

Conflict of Interest

The authors declare no conflict of interest.

Data Availability Statement

The data that support the findings of this study are available on request from the corresponding author. The data are not publicly available due to privacy or ethical restrictions.

Keywords

dendrite-free lithium plating, in situ sum frequency generation (SFG), Li-ion desolvation, lithium-metal batteries, single-atomic catalysts

Received: March 27, 2023

Revised: May 26, 2023

Published online:

- [1] a) J. Wang, L. Li, H. Hu, H. Hu, Q. Guan, M. Huang, L. Jia, H. Adenusi, K. V. Tian, J. Zhang, S. Passerini, H. Lin, *ACS Nano* **2022**, *16*, 17729; b) X. He, D. Bresser, S. Passerini, F. Baakes, U. Krewer, J. Lopez, C. T. Mallia, Y. Shao-Horn, I. Cekic-Laskovic, S. Wiemers-Meyer, F. A. Soto, V. Ponce, J. M. Seminario, P. B. Balbuena, H. Jia, W. Xu, Y. Xu, C. Wang, B. Horstmann, R. Amine, C.-C. Su, J. Shi, K. Amine, M. Winter, A. Latz, R. Kostecki, *Nat. Rev. Mater.* **2021**, *6*, 1036; c) G. Zhou, H. Chen, Y. Cui, *Nat. Energy* **2022**, *7*, 312; d) G. A. Elia, K. Marquardt, K. Hoepfner, S. Fantini, R. Lin, E. Knipping, W. Peters, J. F. Drillet, S. Passerini, R. Hahn, *Adv. Mater.* **2016**, *28*, 7564; e) Y. Zhang, G. Xu, Q. Kang, L. Zhan, W. Tang, Y. Yu, K. Shen, H. Wang, X. Chu, J. Wang, S. Zhao, Y. Wang, L. Ling, S. Yang, *J. Mater. Chem. A* **2019**, *7*, 16812.

- [2] a) P. Albertus, S. Babinec, S. Litzelman, A. Newman, *Nat. Energy* **2017**, *3*, 16; b) Y. Liu, Q. Liu, L. Xin, Y. Liu, F. Yang, E. A. Stach, J. Xie, *Nat. Energy* **2017**, *2*, 17083; c) J. Zhang, C. You, H. Lin, J. Wang, *Energy Environ. Mater.* **2022**, *5*, 731.
- [3] a) C. Niu, H. Pan, W. Xu, J. Xiao, J. G. Zhang, L. Luo, C. Wang, D. Mei, J. Meng, X. Wang, Z. Liu, L. Mai, J. Liu, *Nat. Nanotechnol.* **2019**, *14*, 594; b) C. Yan, H. R. Li, X. Chen, X. Q. Zhang, X. B. Cheng, R. Xu, J. Q. Huang, Q. Zhang, *J. Am. Chem. Soc.* **2019**, *141*, 9422; c) B. Horstmann, J. Shi, R. Amine, M. Werres, X. He, H. Jia, F. Hausen, I. Cekic-Laskovic, S. Wiemers-Meyer, J. Lopez, D. Galvez-Aranda, F. Baakes, D. Bresser, C.-C. Su, Y. Xu, W. Xu, P. Jakes, R.-A. Eichel, E. Figgemeier, U. Krewer, J. M. Seminario, P. B. Balbuena, C. Wang, S. Passerini, Y. Shao-Horn, M. Winter, K. Amine, R. Kostecki, A. Latz, *Energy Environ. Sci.* **2021**, *14*, 5289; d) J. H. Um, S. H. Yu, *Adv. Energy Mater.* **2020**, *11*, 2003004; e) Z. Chen, G. T. Kim, J. K. Kim, M. Zarrabetitua, M. Kuenzel, H. P. Liang, D. Geiger, U. Kaiser, S. Passerini, *Adv. Energy Mater.* **2021**, *11*, 2101339.
- [4] a) B. Liu, J.-G. Zhang, W. Xu, *Joule* **2018**, *2*, 833; b) Q. Kang, Z. C. Zhuang, Y. Li, Y. Z. Zuo, J. Wang, Y. J. Liu, C. Q. Shi, J. Chen, H. F. Li, P. K. Jiang, X. Y. Huang, *Nano Res.* **2023**, *16*, 9240; c) Z. Chen, D. Steinle, H.-D. Nguyen, J.-K. Kim, A. Mayer, J. Shi, E. Paillard, C. Iojoiu, S. Passerini, D. Bresser, *Nano Energy* **2020**, *77*, 105129.
- [5] a) R. Fang, S. Zhao, Z. Sun, D. W. Wang, H. M. Cheng, F. Li, *Adv. Mater.* **2017**, *29*, 1606823; b) Y. Hu, L. Li, H. Tu, X. Yi, J. Wang, J. Xu, W. Gong, H. Lin, X. Wu, M. Liu, *Adv. Funct. Mater.* **2022**, *32*, 2203336; c) M. Salama, R. A. Rosy, R. Yemini, Y. Gofer, D. Aurbach, M. Noked, *ACS Energy Lett.* **2019**, *4*, 436.
- [6] a) D. Wang, C. Luan, W. Zhang, X. F. Liu, L. S. Sun, Q. Liang, T. T. Qin, Z. Z. Zhao, Y. Zhou, P. Wang, W. T. Zheng, *Adv. Energy Mater.* **2018**, *8*, 1800650; b) D. Wang, Y. Liu, G. Li, C. Qin, L. Huang, Y. Wu, *Adv. Funct. Mater.* **2021**, *31*, 2106740; c) L. P. Hou, N. Yao, J. Xie, P. Shi, S. Y. Sun, C. B. Jin, C. M. Chen, Q. B. Liu, B. Q. Li, X. Q. Zhang, Q. Zhang, *Angew. Chem., Int. Ed.* **2022**, *61*, e202201406; d) J. Wang, H. Hu, S. Duan, Q. Xiao, J. Zhang, H. Liu, Q. Kang, L. Jia, J. Yang, W. Xu, H. Fei, S. Cheng, L. Li, M. Liu, H. Lin, Y. Zhang, *Adv. Funct. Mater.* **2021**, *32*, 2110468; e) J. Wang, S. Cheng, L. Li, L. Jia, J. Wu, X. Li, Q. Guan, H. Hu, J. Zhang, H. Lin, *Chem. Eng. J.* **2022**, *446*, 137291; f) J. Wang, H. Hu, J. Zhang, L. Li, L. Jia, Q. Guan, H. Hu, H. Liu, Y. Jia, Q. Zhuang, S. Cheng, M. Huang, H. Lin, *Energy Storage Mater.* **2022**, *52*, 210; g) H. Wang, M. Matsui, H. Kuwata, H. Sonoki, Y. Matsuda, X. Shang, Y. Takeda, O. Yamamoto, N. Imanishi, *Nat. Commun.* **2017**, *8*, 15106; h) Y. Liu, D. Lin, P. Y. Yuen, K. Liu, J. Xie, R. H. Dauskardt, Y. Cui, *Adv. Mater.* **2017**, *29*, 1605531; i) Q. Li, S. Zhu, Y. Lu, *Adv. Funct. Mater.* **2017**, *27*, 1606422; j) S. Choudhury, Z. Tu, S. Stalin, D. Vu, K. Fawole, D. Gunceler, R. Sundararaman, L. A. Archer, *Angew. Chem., Int. Ed.* **2017**, *56*, 13070; k) H. Tu, L. Li, Z. Wang, J. Wang, H. Lin, M. Wang, C. Yan, M. Liu, *ACS Nano* **2022**, *16*, 16898.
- [7] a) Z. A. Ghazi, Z. Sun, C. Sun, F. Qi, B. An, F. Li, H. M. Cheng, *Small* **2019**, *15*, 1900687; b) Y. Zhang, Z. Cao, S. Liu, Z. Du, Y. Cui, J. Gu, Y. Shi, B. Li, S. Yang, *Adv. Energy Mater.* **2022**, *12*, 2103979; c) Q. Kang, Y. Li, Z. Zhuang, D. Wang, C. Zhi, P. Jiang, X. Huang, *J. Energy Chem.* **2022**, *69*, 194.
- [8] a) J. Wang, J. Zhang, S. Duan, L. Jia, Q. Xiao, H. Liu, H. Hu, S. Cheng, Z. Zhang, L. Li, W. Duan, Y. Zhang, H. Lin, *Nano Lett.* **2022**, *22*, 8008; b) J. Wang, J. Zhang, S. Cheng, J. Yang, Y. Xi, X. Hou, Q. Xiao, H. Lin, *Nano Lett.* **2021**, *21*, 3245; c) J. Zhang, R. He, Q. Zhuang, X. Ma, C. You, Q. Hao, L. Li, S. Cheng, L. Lei, B. Deng, X. Li, H. Lin, J. Wang, *Adv. Sci.* **2022**, *9*, e2202244.
- [9] a) Z. Chang, Y. Qiao, H. Deng, H. Yang, P. He, H. Zhou, *Joule* **2020**, *4*, 1776; b) Z. Chang, Y. Qiao, H. Yang, H. Deng, X. Zhu, P. He, H. Zhou, *Energy Environ. Sci.* **2020**, *13*, 4122.
- [10] a) Z. Chang, Y. Qiao, H. Yang, X. Cao, X. Zhu, P. He, H. Zhou, *Angew. Chem., Int. Ed.* **2021**, *60*, 15572; b) Z. Chang, H. Yang, X. Zhu, P. He, H. Zhou, *Nat. Commun.* **2022**, *13*, 1510; c) L. Suo, Y. S. Hu, H. Li, M. Armand, L. Chen, *Nat. Commun.* **2013**, *4*, 1481; d) L. Fu, X. Wang, L. Wang, M. Wan, Y. Li, Z. Cai, Y. Tan, G. Li, R. Zhan, Z. W. Seh, Y. Sun, *Adv. Funct. Mater.* **2021**, *31*, 2010602; e) G. M. A. Girard, M. Hilder, D. Nucciarone, K. Whitbread, S. Zavorine, M. Moser, M. Forsyth, D. R. MacFarlane, P. C. Howlett, *J. Phys. Chem. C* **2017**, *121*, 21087; f) L. Sheng, Q. Wang, X. Liu, H. Cui, X. Wang, Y. Xu, Z. Li, L. Wang, Z. Chen, G. L. Xu, J. Wang, Y. Tang, K. Amine, H. Xu, X. He, *Nat. Commun.* **2022**, *13*, 172.
- [11] M. Zhu, B. Li, S. Li, Z. Du, Y. Gong, S. Yang, *Adv. Energy Mater.* **2018**, *8*, 1703505.
- [12] a) J. Wang, L. Jia, S. Duan, H. Liu, Q. Xiao, T. Li, H. Fan, K. Feng, J. Yang, Q. Wang, M. Liu, J. Zhong, W. Duan, H. Lin, Y. Zhang, *Energy Storage Mater.* **2020**, *28*, 375; b) J. Wang, L. Jia, J. Zhong, Q. Xiao, C. Wang, K. Zang, H. Liu, H. Zheng, J. Luo, J. Yang, H. Fan, W. Duan, Y. Wu, H. Lin, Y. Zhang, *Energy Storage Mater.* **2019**, *18*, 246; c) J. Wang, L. Jia, H. Lin, Y. Zhang, *ChemSusChem* **2020**, *13*, 3404.
- [13] a) Y. Zhang, L. Guo, L. Tao, Y. Lu, S. Wang, *Small Methods* **2018**, *3*, 1800406; b) J. Wan, W. Chen, C. Jia, L. Zheng, J. Dong, X. Zheng, Y. Wang, W. Yan, C. Chen, Q. Peng, D. Wang, Y. Li, *Adv. Mater.* **2018**, *30*, 1705369; c) L. Zhang, X. Zhao, Z. Yuan, M. Wu, H. Zhou, *J. Mater. Chem. A* **2021**, *9*, 3855.
- [14] a) J. Wang, L. Jia, H. Liu, C. Wang, J. Zhong, Q. Xiao, J. Yang, S. Duan, K. Feng, N. Liu, W. Duan, H. Lin, Y. Zhang, *ACS Appl. Mater. Interfaces* **2020**, *12*, 12727; b) S. Cheng, J. Wang, S. Duan, J. Zhang, Q. Wang, Y. Zhang, L. Li, H. Liu, Q. Xiao, H. Lin, *Chem. Eng. J.* **2021**, *417*, 128172.
- [15] F. Liu, Q. Yu, J. Xue, B. Shu, C. Zheng, H. Deng, X. Zhang, P. Gong, M. Chen, H. Lin, J. Wang, S. Zhu, J. Wu, *J. Phys. Chem. Lett.* **2022**, *13*, 9501.
- [16] M. Jäckle, K. Helmbrecht, M. Smits, D. Stottmeister, A. Groß, *Energy Environ. Sci.* **2018**, *11*, 3400.
- [17] a) M. M. Millet, G. Algara-Siller, S. Wrabetz, A. Mazheika, F. Girgsdies, D. Teschner, F. Seitz, A. Tarasov, S. V. Levchenko, R. Schlögl, E. Frei, *J. Am. Chem. Soc.* **2019**, *141*, 2451; b) Y. Li, P. Xu, J. Mou, S. Xue, S. Huang, J. Hu, Q. Dong, C. Yang, M. Liu, *Small Methods* **2021**, *5*, 2100833.
- [18] X. Lian, N. Xu, Y. Ma, F. Hu, H. Wei, H.-Y. Chen, Y. Wu, L. Li, D. Li, S. Peng, *Chem. Eng. J.* **2021**, *421*, 127755.
- [19] J. Wang, S. Cheng, W. Li, S. Zhang, H. Li, Z. Zheng, F. Li, L. Shi, H. Lin, Y. Zhang, *J. Power Sources* **2016**, *321*, 193.
- [20] a) Y. Xi, X. Ye, S. Duan, T. Li, J. Zhang, L. Jia, J. Yang, J. Wang, H. Liu, Q. Xiao, *J. Mater. Chem. A* **2020**, *8*, 14769; b) S. Shit, S. Chhetri, W. Jiang, N. C. Murmu, H. Koo, P. Samanta, T. Kuila, *ACS Appl. Mater. Interfaces* **2018**, *10*, 27712.
- [21] Y. Chen, S. Ji, Y. Wang, J. Dong, W. Chen, Z. Li, R. Shen, L. Zheng, Z. Zhuang, D. Wang, Y. Li, *Angew. Chem., Int. Ed.* **2017**, *56*, 6937.
- [22] a) Y. R. Shen, *Nature* **1989**, *337*, 519; b) K. B. Eisenthal, *Chem. Rev.* **1996**, *96*, 1343.
- [23] J. Wang, J. Yang, Q. Xiao, J. Zhang, T. Li, L. Jia, Z. Wang, S. Cheng, L. Li, M. Liu, H. Liu, H. Lin, Y. Zhang, *Adv. Funct. Mater.* **2020**, *31*, 2007434.
- [24] Y. Horowitz, H. L. Han, P. N. Ross, G. A. Somorjai, *J. Am. Chem. Soc.* **2016**, *138*, 726.
- [25] a) H. Zhang, F. Li, Q. Xiao, H. Lin, *J. Phys. Chem. Lett.* **2015**, *6*, 2170; b) Y. Xi, Q. Xiao, J. Du, X. Ye, X. Kong, Z. Chang, T. Li, H. Jin, J. Wang, H. Lin, *Adv. Mater. Interfaces* **2020**, *7*, 1902046.
- [26] J. Xu, S. An, X. Song, Y. Cao, N. Wang, X. Qiu, Y. Zhang, J. Chen, X. Duan, J. Huang, W. Li, Y. Wang, *Adv. Mater.* **2021**, *33*, 2105178.
- [27] G. Zhou, S. Zhao, T. Wang, S. Z. Yang, B. Johannessen, H. Chen, C. Liu, Y. Ye, Y. Wu, Y. Peng, C. Liu, S. P. Jiang, Q. Zhang, Y. Cui, *Nano Lett.* **2020**, *20*, 1252.